


# Synthesis, Characterization, and Photocatalytic Properties of Flower-like Mn-doped Ceria

Pei Li<sup>ab</sup>, Wei Zhang<sup>a</sup>, Xun Zhang<sup>a</sup>, Zhengde Wang<sup>a</sup>, Xianpeng Wang<sup>a</sup>, Songlin Ran<sup>b</sup>, Yaohui Lv<sup>a\*</sup> 

<sup>a</sup>School of Materials Science and Engineering, Anhui Key Laboratory of Metal Materials and Processing, Anhui University of Technology, Anhui, Maanshan, 243002, China

<sup>b</sup>Key Laboratory of Metallurgical Emission Reduction & Resources Recycling, Ministry of Education, Anhui University of Technology, Anhui, Maanshan, 243002, China

Received: March 05, 2018; Revised: May 22, 2018; Accepted: June 08, 2018

Mn-doped CeO<sub>2</sub> flower-like microstructures have been synthesized by a facile one-step composite-hydroxide-mediated method. The structure, morphology, optical and the surface properties of Mn doped CeO<sub>2</sub> have been investigated by X-ray diffraction (XRD), field-emission scanning electron microscopy (FESEM), UV-Vis absorption spectroscopy and X-ray photoelectron spectroscopy (XPS). The XRD results confirmed the successful incorporation of Mn into the CeO<sub>2</sub> lattice through the formation of face-centered cubic solid solution. The photocatalytic activities of the catalysts were evaluated by measuring the photodegradation efficiency of Rhodamine B (RhB) under ultraviolet light irradiation. With an optimal molar ratio of 1% in Mn/CeO<sub>2</sub> the highest rate photodegradation was achieved under the experimental conditions. The enhanced photocatalytic activity can be attributed to the incorporation of multivalent Mn in CeO<sub>2</sub> promoted the separation of photogenerated charges, inhibited the recombination of photogenerated carriers, and thus prolonged the charges lifetime to participate in the photocatalytic reaction.

**Keywords:** Cerium oxide, Manganese doped, Photocatalysis.

## 1. Introduction

Semiconductor-based photocatalysis has emerged as one of the most attractive techniques to convert sunlight into chemical energy so as to remove organic pollutants from wastewater for environmental remediation. Among various semiconductor materials, as a high-efficiency, nontoxicity, abundant, photochemical stability and low-cost promising photocatalyst, CeO<sub>2</sub> has been an extensively investigated material for environmental pollution removal and photocatalytic hydrogen evolution<sup>1-3</sup>. Nevertheless, some drawbacks limit its practical application in the photocatalyst region, including rapid recombination rate of photogenerated electron-hole pairs, low quantum yield in the reactions, and very poor response to visible light. Therefore, from the viewpoint of photochemistry, numerous methods for suppression of these drawbacks have been attempted to improve CeO<sub>2</sub>-based photocatalytic activities. To the best of our knowledge, one of approaches is to develop CeO<sub>2</sub> based heterostructure semiconductor systems, such as TiO<sub>2</sub>@Pt@CeO<sub>2</sub><sup>4</sup>, Au/CeO<sub>2</sub><sup>5,6</sup>, CdS/CeO<sub>2</sub><sup>7</sup>, SrTiO<sub>3</sub>/CeO<sub>2</sub><sup>8</sup>, Bi<sub>2</sub>O<sub>3</sub>/CeO<sub>2</sub><sup>9</sup>, TiO<sub>2</sub>/CeO<sub>2</sub><sup>10,11</sup> and Cu<sub>2</sub>O/CeO<sub>2</sub><sup>12</sup>. On the other hand, there have been modifications of CeO<sub>2</sub> by doping non-metallic species<sup>13,14</sup> and crystal facet engineering<sup>15,16</sup>. For instance, Zhu et al.<sup>13</sup> reported the synthesis of N-doped CeO<sub>2</sub> nanoparticles with controllable doping levels at the nanoscale through a reliable wet chemical approach, showing enhanced visible-light sensitivity and photocatalytic activity. Fuertes et al.<sup>14</sup> have doped nitrogen into ceria powder by sintering CeO<sub>2</sub>

in NH<sub>3</sub> flow at very high temperature. Recent reports have shown that CeO<sub>2</sub> nanostructures with highly active exposed crystal planes such as {100} and {110} can significantly enhance their catalytic activity<sup>15</sup>. Meanwhile, the selective metal doping of CeO<sub>2</sub> to improve its performance started to appear in the literature. Recently, the metal doping of CeO<sub>2</sub> has also been examined in solar cell devices<sup>17</sup>, but the corresponding photocatalytic investigations are relatively few.

It has been reported that doping with multivalent transition-metal (TM) cations was considered an effective method to inhibit the recombination of photogenerated carriers in semiconductors<sup>18</sup>. Theoretical investigation showed that among the 3d metals, Mn has the greatest potential in permitting significant optical absorption in the visible or even the infrared solar light, through the combined effects of narrowed band gap and the introduction of intermediate bands within the forbidden gap<sup>19,20</sup>. Recently, there have been many reports on Mn-doped oxide photo-activity under UV and visible light, such as Mn-ZnO<sup>21-24</sup>, Mn-TiO<sub>2</sub><sup>25,26</sup>, where Mn exists in the bivalence oxidation state.

Inspired by above-mentioned investigations, flower-like Mn-doped CeO<sub>2</sub> photocatalyst was obtained via a simple one-step composite-hydroxide-mediated method. In addition, we demonstrated the enhanced photocatalytic performance of the Mn doped CeO<sub>2</sub> flower-like nanostructures by degradation of Rhodamine B (RhB) solutions, and further investigated the impact of Mn doping concentrations of doped CeO<sub>2</sub> on the resulting photocatalytic activities under ultraviolet light.

\*e-mail: 396839980@qq.com.

## 2. Experimental

### 2.1 Material preparation

Pure and flower-like Mn-doped CeO<sub>2</sub> nanostructure were obtained by a simple one-step composite-hydroxide-mediated method according to our group previously report with tiny modification<sup>27</sup>. In a typical preparation process, (1) a total of 20 g of KOH and KI was mixed at a ratio of 70.6:29.4 and placed in a 25mL Teflon vessel. (2) Different molar ratio of MnSO<sub>4</sub>·H<sub>2</sub>O and CeO<sub>2</sub> was used as the raw material for reaction, and was placed on the top of the hydroxide in the vessel. (3) The Teflon vessel was put into a furnace preheated to 235 °C. (4) After the hydroxide was totally molten (30 min later), the molten reactants were mixed uniformly by shaking the covered vessel. (5) 24 hours later, the vessel was taken out and cooled to room temperature naturally. The as-prepared samples were removed from the solution, rinsed thoroughly several times with deionized water and ethanol to remove residual salts, and subsequently dried for 12h at vacuum circumstance. The as-prepared samples in the subsequent discussion in this paper are denoted as x% Mn/CeO<sub>2</sub>, where x% refers to the Mn/(Mn+Ce) molar ratio.

### 2.2 Catalyst characterization

The crystal structure of the resultant products was characterized by X-ray powder diffraction (XRD) by using a Bruker AXS D8 advance powder diffractometer with Cu K $\alpha$  radiation ( $\lambda = 0.154056$  nm). Field-emission scanning electron microscope (FESEM, S-4800) was employed to characterize the morphologies and size of the synthesized Mn doped CeO<sub>2</sub> samples. UV-vis diffuse reflectance spectra were obtained for the dry-pressed disk samples by using a Shimadzu UV 2550 recording spectrophotometer, which was equipped with an integrating sphere, and BaSO<sub>4</sub> was used as a reference. X-ray photoelectron spectroscopy (XPS) measurements were performed on a Thermo Fisher Scientific Escalab 250 spectrometer with monochromatized Al K $\alpha$  excitation, and C<sub>1s</sub> (284.6 eV) was used to calibrate the peak positions of the elements. The Raman-scattering experiments were carried out using NEXUS 670 Raman spectrometer at room temperature. The 473 nm line of the solid-state laser was used for excitation.

### 2.3 Catalyst activity

The photocatalytic performance of the as-prepared samples was characterized by decomposing RhB under ultraviolet light irradiation at room temperature. The photocatalytic experiments were carried out by adding 100 mg photocatalysts into 300 mL of 10 mg L<sup>-1</sup> RhB solution in the vessel. A 300 W Hg arc lamp (XPA-1, Nanjing XuJiang Electromechanical Plant) was used as the light source. Prior to the irradiation, the suspensions were magnetically stirred in the dark for 30 min to establish the adsorption/desorption equilibrium.

After different irradiation time, the concentration of the RhB solution was measured on a UV-Vis spectrophotometer (Hitachi UV-3100).

## 3. Results and Discussion

The X-ray diffraction (XRD) patterns of Mn<sub>x</sub>Ce<sub>1-x</sub>O<sub>2</sub> photocatalysts are shown in Figure 1 along with pure CeO<sub>2</sub>. The diffraction peaks of pure CeO<sub>2</sub> can be indexed to the fluorite cubic phase of CeO<sub>2</sub> (JCPDF card: 65-2975) with lattice constant  $a = 0.5411$  nm. The diffraction pattern of Mn<sub>x</sub>Ce<sub>1-x</sub>O<sub>2</sub> photocatalysts was similar to that of pure CeO<sub>2</sub>. The XRD pattern does not show any impurity/additional peaks for any Mn doping concentration. This clearly confirms that the Mn ions occupy positions within the fluorite-lattice. Furthermore, the extended X-ray diffraction pattern of Mn<sub>x</sub>Ce<sub>1-x</sub>O<sub>2</sub> photocatalysts reveals a slight shift in the peak positions towards larger angles with increasing Mn-concentration, which may be due to the lattice reduction of CeO<sub>2</sub> upon Mn ions doping. Because the ionic radius of Mn<sup>n+</sup> (Mn<sup>4+</sup>=0.53 Å, Mn<sup>3+</sup>=0.645 Å, Mn<sup>2+</sup>=0.83 Å) is smaller than that of Ce<sup>4+</sup> (1.01 Å), when Mn<sup>n+</sup> embedded in CeO<sub>2</sub> lattice and takes the place of Ce<sup>4+</sup>, the contraction and distortion of the ceria lattice occur, leading to the decrease of the cell parameter<sup>28</sup>. In present study, the existence of the Mn<sup>n+</sup> oxidation state in Mn<sub>x</sub>Ce<sub>1-x</sub>O<sub>2</sub> photocatalysts will be discussed in the later section.

Figure 2 shows the morphology and size of the source material CeO<sub>2</sub> (a) and the flower-like 1% Mn-doped CeO<sub>2</sub> sample (b) obtained by typical field-emission scanning electron microscope (FESEM). The anomalous particles morphology of the source material CeO<sub>2</sub> can be seen with the diameter ranging from 2-8  $\mu$ m (Figure 2 a). From the high-magnification SEM images shown in Figure 2 b, it can be seen that the flower-like micro-/nano-architectures are

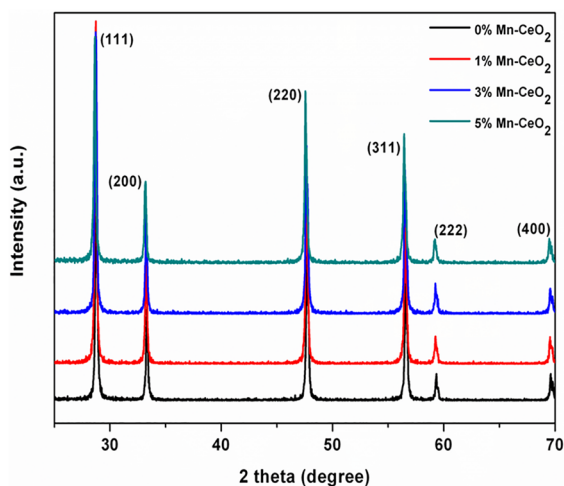


**Figure 1.** XRD patterns of Mn-doped CeO<sub>2</sub> from different mole concentrations of Mn source

built from dozens of flake-like nanopetals with the average diameter of 1-4  $\mu\text{m}$ .

The effect of Mn substitution on cubic fluorite structure of  $\text{CeO}_2$  lattice is further confirmed using UV-visible optical spectroscopy measured in the range of 200-800 nm. Figure 3a shows the room-temperature optical absorption spectra of undoped and flower-like Mn-doped  $\text{CeO}_2$  photocatalyst. The absorbance spectra for 1 % Mn-doped  $\text{CeO}_2$  sample was found to increase when compared to the undoped  $\text{CeO}_2$  sample. However, the absorbance intensity for the 3 and 5% Mn-doped  $\text{CeO}_2$  sample were found to decrease when compared to the undoped  $\text{CeO}_2$  sample. This may be due to the electron-electron, electron-donor atom and electron-hole interactions which increase drastically as doping is increased beyond a critical limit<sup>29,30</sup>. These interactions dominate the electron-photon interactions. A plot of variation of  $(\alpha h\nu)^2$  versus  $h\nu$ , which is obtained according to the Kubelka-Munk function transformation, is shown in

Figure 3 b. The evaluated band gap values for the pure and the 1% Mn-doped  $\text{CeO}_2$  sample were observed to be 3.05 eV and 2.88 eV, respectively. It could be seen that the band gap value slightly decreased when the dopant concentration of Mn was increased.

Raman scattering is an effective tool for the investigation of the effects of doping on nanomaterials, as the incorporation of dopants leads to shifts of the lattice Raman vibrational peak positions. Figure 4 displays the Raman spectra of pure  $\text{CeO}_2$  as well as Mn-doped  $\text{CeO}_2$  samples with different Mn contents. For the pure  $\text{CeO}_2$  sample, a strong peak at  $461\text{ cm}^{-1}$  can be assigned to the  $F_{2g}$  Raman active mode of the cubic fluorite structure of  $\text{CeO}_2$ , which is due to the symmetric breathing mode of the oxygen atoms around cerium ions. Compared to the pure  $\text{CeO}_2$ , the peak intensity decreased greatly and became broader and red-shifted for the Mn-doped  $\text{CeO}_2$  samples. The red-shift could be attributed to the changes in lattice parameter with crystallite size, as it

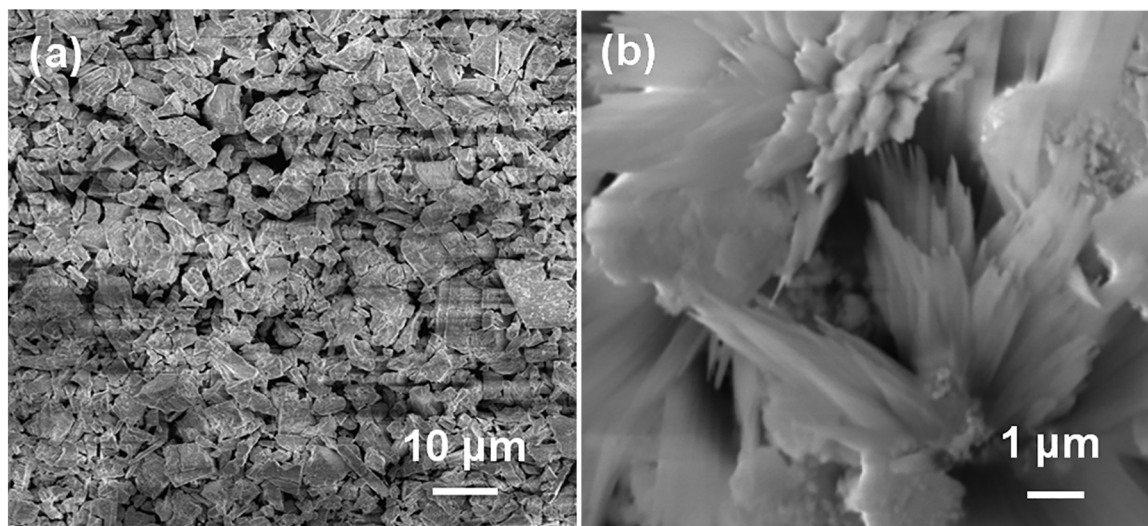


Figure 2. FESEM images of (a) pure  $\text{CeO}_2$  raw materials; (b) 1% Mn/ $\text{CeO}_2$  sample

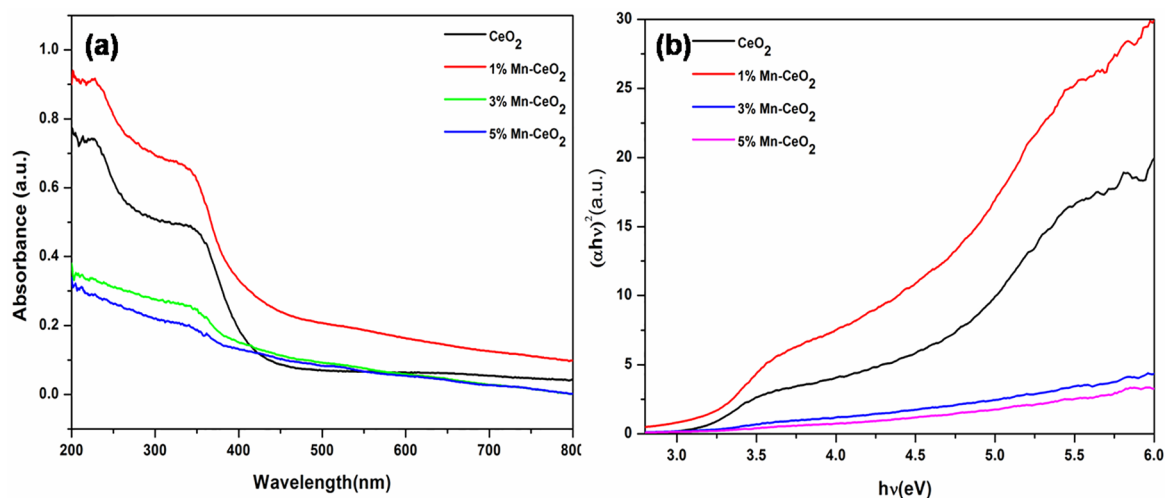
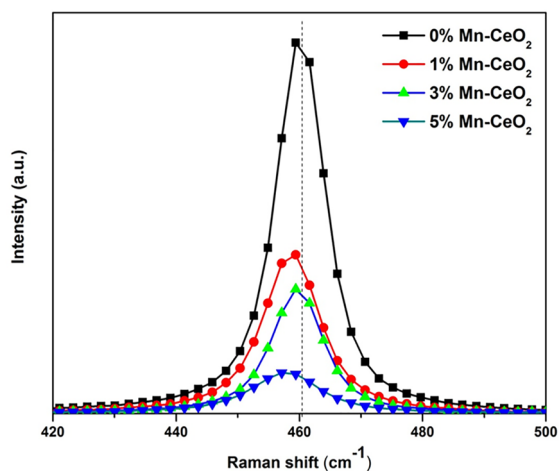


Figure 3. (a) UV-Vis absorption spectra of Mn/ $\text{CeO}_2$  with varying Mn/Ce molar ratio; (b) Plot of  $(\alpha h\nu)^2$  versus photon energy of pure and Mn-doped  $\text{CeO}_2$  samples



**Figure 4.** Raman spectra of Mn/CeO<sub>2</sub> with varying Mn/Ce molar ratio

was previously explained by phonon confinement model<sup>31,32</sup>. Another reason of shifting and broadening may be the increase in oxygen vacancies, which is related to structural defects derived from partially incorporation of manganese into CeO<sub>2</sub> lattice. In the Mn-doped CeO<sub>2</sub> samples, the extra oxygen vacancies were generated by the incorporation of Mn ion into the ceria fluorite lattice to compensate for the valence mismatch between the Mn<sup>n+</sup> and Ce<sup>4+</sup> ions.

The chemical states of the Mn doping in the as-prepared samples were then investigated by XPS, as presented in Figure 5a, the XPS survey spectra indicated that the as-prepared Mn doped CeO<sub>2</sub> nanoflowers were composed of Ce, O and Mn elements. Figure 5b shows the XPS spectra of the Mn 2p region. The double peaks with binding energies of ca. 641.0 eV and 653.1 eV correspond to the characteristic of Mn 2p<sub>3/2</sub> and Mn 2p<sub>1/2</sub> signals, respectively. Since XPS signals for Mn<sup>2+</sup> and Mn<sup>3+</sup> are very close to each other ~ 641.0 eV for the BE of Mn 2p<sub>3/2</sub>,<sup>33</sup> thus the coexistence of Mn<sup>2+</sup>/

Mn<sup>3+</sup> ion couple in the Mn-doped CeO<sub>2</sub> samples. Here, the Mn 2p<sub>3/2</sub> peak is deconvoluted with the Gaussian-Lorentz model functions, and two peaks at 641.2 eV and 642.3 eV can be assigned to the Mn<sup>2+</sup> and Mn<sup>3+</sup> ions, respectively, according to the standard binding energy and previous literature.<sup>3</sup> This results suggest the coexistence of Mn<sup>2+</sup> and Mn<sup>3+</sup> ions on the surface of samples. In addition, we can observe that the XPS peaks show some noise, implying that the content of Mn ions at the surface of the sample is low and Mn ions have been doped into the interior of the nanostructure.

The effective incorporation of Mn<sup>2+</sup> ions into CeO<sub>2</sub> crystalline lattices can greatly enhance the light photocatalytic performance. The UV-vis spectral changes of RhB solution over 1% Mn doped CeO<sub>2</sub> samples during the photodegradation are shown in Figure 6a, clearly show that the characteristic absorption peaks corresponding to RhB decrease rapidly as the exposure time increases, indicating the decomposition of RhB and the significant reduction in the RhB concentration. Figure 6 b shows the results of RhB photodegradation over Mn doped CeO<sub>2</sub> samples with different Mn doping concentrations. After 210 min of irradiation, the photodegradation efficiencies of RhB were about 65, 40 and 30% for 1, 3 and 5% Mn doped CeO<sub>2</sub> samples, respectively. It was evident that 1% Mn doped CeO<sub>2</sub> samples exhibited excellent photocatalytic activities for the RhB degradation. However, the photocatalytic performance of Mn doped CeO<sub>2</sub> samples decreased with the increase of Mn doped amount. The results show that there was an optimal Mn doping concentration in CeO<sub>2</sub> samples for the ultraviolet light photocatalysis (1% Mn dopant). When the Mn doping concentration was further increased, the Mn dopant sites could be also act as efficient recombination centers with increased recombination rate due to the reduced average distance between trapped carriers<sup>34</sup>. The excess Mn dopant sites could greatly decrease the number of charge carriers and deteriorate the photocatalytic performance of doped CeO<sub>2</sub> samples, as identified from Figure 6b.

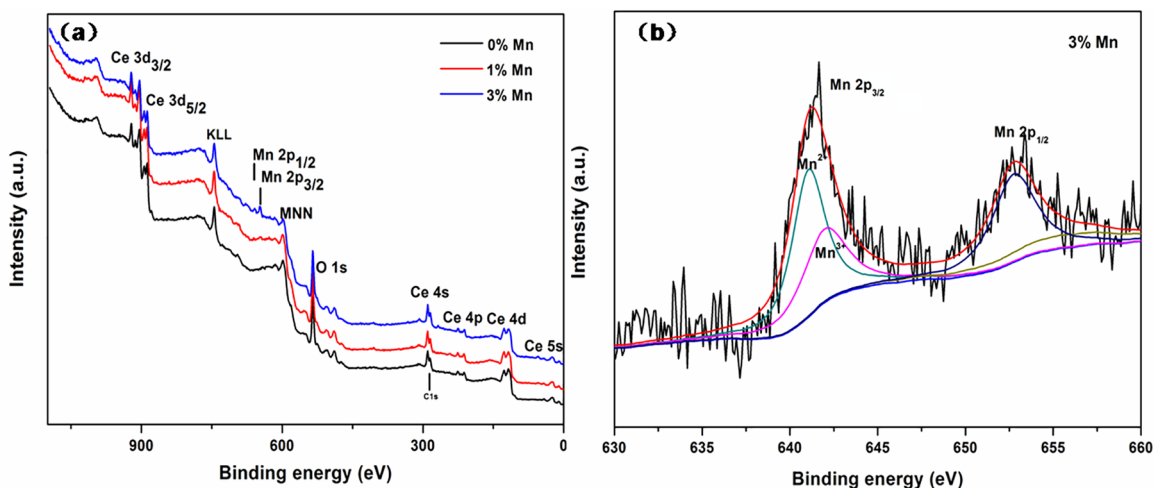


**Figure 5.** XPS spectra (a) survey spectrum and (b) Mn 2p for 3% Mn/CeO<sub>2</sub> sample

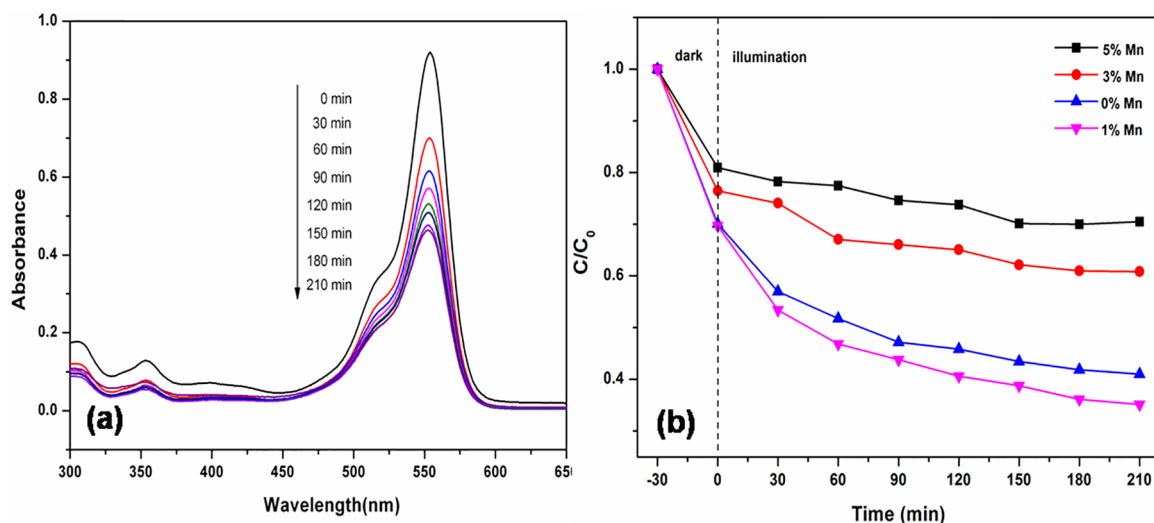


**Figure 6.** (a) UV-vis spectral variations of RhB solution over 1% Mn doped CeO<sub>2</sub> under ultraviolet light irradiation; (b) Degradation of RhB solutions over CeO<sub>2</sub> and Mn doped CeO<sub>2</sub> with different Mn concentrations under ultraviolet light

## 4. Conclusions

In summary, we have synthesized a series of Mn/CeO<sub>2</sub> photocatalysts by a facile one-step composite-hydroxide-mediated approach. This work focuses on understanding of the effects of the Mn addition in Mn-doped CeO<sub>2</sub> nanoflowers. Noticeably, there was an optimal Mn doping concentration in CeO<sub>2</sub> samples for the ultraviolet light photocatalysis. Experiments showed that 1% Mn-doped CeO<sub>2</sub> had higher photocatalytic capability compared with that of the pure CeO<sub>2</sub> or 3% and 5% Mn ion-doping catalyst. The enhancement in redox efficiency of CeO<sub>2</sub> samples upon Mn doping may be due to the increase in charge transport rate.

## 5. Acknowledgements

This research was financially supported by the Natural Science Foundation of Anhui Provincial Education Department (KJ2016A102), Anhui Provincial Natural Science Foundation (1808085ME138), Graduate student Innovation Fund of Anhui University of Technology and National Undergraduate Training Programs for Innovation and Entrepreneurship (201710360024, 201710360026)

## 6. References

- Li L, Wang HR, Zou L, Wang X. Controllable synthesis, photocatalytic and electrocatalytic properties of CeO<sub>2</sub> nanocrystals. *RSC Advances*. 2015;5(52):41506-41512.
- Lu X, Zhai T, Cui H, Shi J, Xie S, Huang Y, et al. Redox cycles promoting photocatalytic hydrogen evolution of CeO<sub>2</sub> nanorods. *Journal of Materials Chemistry*. 2011;21(15):5569-5572.
- Rangaswamy A, Venkataswamy P, Devaiah D, Ramana S, Reddy BM. Structural characteristics and catalytic performance of nanostructured Mn-doped CeO<sub>2</sub> solid solutions towards oxidation of benzylamine by molecular O<sub>2</sub>. *Materials Research Bulletin*. 2017;88:136-147.
- Li SX, Cai JB, Wu XQ, Liu BW, Chen QY, Li YH, et al. TiO<sub>2</sub>@Pt@CeO<sub>2</sub> nanocomposite as a bifunctional catalyst for enhancing photo-reduction of Cr (VI) and photo-oxidation of benzyl alcohol. *Journal of Hazardous Materials*. 2018;346:52-61.
- Li BX, Zhang BS, Nie SB, Shao LZ, Hu LY. Optimization of plasmon-induced photocatalysis in electrospun Au/CeO<sub>2</sub> hybrid nanofibers for selective oxidation of benzyl alcohol. *Journal of Catalysis*. 2017;348:256-264.
- Tanaka A, Hashimoto K, Kominami H. Selective photocatalytic oxidation of aromatic alcohols to aldehydes in an aqueous suspension of gold nanoparticles supported on cerium(IV) oxide under irradiation of green light. *Chemical Communications*. 2011;47(37):10446-10448.
- Zhang P, Liu Y, Tian BZ, Luo YS, Zhang JL. Synthesis of core-shell structured CdS @CeO<sub>2</sub> and CdS @TiO<sub>2</sub> composites and comparison of their photocatalytic activities for the selective oxidation of benzyl alcohol to benzaldehyde. *Catalysis Today*. 2017;281(Pt 1):181-188.
- Song S, Xu L, He Z, Ying H, Chen J, Xiao X, et al. Photocatalytic degradation of C.I. Direct Red 23 in aqueous solutions under UV irradiation using SrTiO<sub>3</sub>/CeO<sub>2</sub> composite as the catalyst. *Journal of Hazardous Materials*. 2008;152(3):1301-1308.
- Zou ZJ, Xie CS, Zhang SS, Yu XL, Zou T, Li J. Preparation and photocatalytic activity of TiO<sub>2</sub>/CeO<sub>2</sub>/Bi<sub>2</sub>O<sub>3</sub> composite for Rhodamine B degradation under visible light irradiation. *Journal of Alloys and Compounds*. 2013;581:385-391.
- Lu XW, Li XZ, Qian JC, Miao NW, Yao C, Chen ZG. Synthesis and characterization of CeO<sub>2</sub>/TiO<sub>2</sub> nanotube arrays and enhanced photocatalytic oxidative desulfurization performance. *Journal of Alloys and Compounds*. 2016;661:363-371.
- Pavasupree S, Suzuki Y, Pivsa-Art S, Yoshikawa S. Preparation and characterization of mesoporous TiO<sub>2</sub>-CeO<sub>2</sub> nanopowders

- respond to visible wavelength. *Journal of Solid State Chemistry*. 2005;178(1):128-134.
12. Hu S, Zhou F, Wang L, Zhang J. Preparation of Cu<sub>2</sub>O/CeO<sub>2</sub> heterojunction photocatalyst for the degradation of Acid Orange 7 under visible light irradiation. *Catalysis Communications*. 2011;12(9):794-797.
  13. Mao C, Zhao Y, Qiu X, Zhu J, Burda C. Synthesis, characterization and computational study of nitrogen-doped CeO<sub>2</sub> nanoparticles with visible-light activity. *Physical Chemistry Chemical Physics*. 2008;10(36):5633-5638.
  14. Belén Jorge A, Fraxedas J, Cantarero A, Williams AJ, Rodgers J, Atfield JP, et al. Nitrogen doping of ceria. *Chemistry of Materials*. 2008;20(5):1682-1684.
  15. Zhou K, Wang X, Sun X, Peng Q, Li Y. Enhanced catalytic activity of ceria nanorods from well-defined reactive crystal planes. *Journal of Catalysis*. 2005;229(1):206-212.
  16. Ren J, Liu X, Gao RH, Dai WL. Morphology and crystal-plane effects of Zr-doped CeO<sub>2</sub> nanocrystals on the epoxidation of styrene with tert-butylhydroperoxide as the oxidant. *Journal of Energy Chemistry*. 2017;26(4):681-687.
  17. Corma A, Atienzar P, Garcia H, Chane-Ching JY. Hierarchically mesostructured doped CeO<sub>2</sub> with potential for solar-cell use. *Nature Materials*. 2004;3(6):394-397.
  18. Prabakaran DDM, Sadaiyandi K, Mahendran M, Sagadevan S. Investigating the effect of Mn-doped CeO<sub>2</sub> nanoparticles by co-precipitation method. *Applied Physics A*. 2018;124(2):86.
  19. Shao G. Electronic structures of manganese-doped rutile TiO<sub>2</sub> from first principles. *The Journal of Physical Chemistry C*. 2008;112(47):18677-18685.
  20. Shao G. Red shift in manganese- and iron-doped TiO<sub>2</sub>: a DFT+U analysis. *The Journal of Physical Chemistry C*. 2009;113(16):6800-6808.
  21. Yang Y, Li Y, Zhu L, He H, Hu L, Huang J, et al. Shape control of colloidal Mn doped ZnO nanocrystals and their visible light photocatalytic properties. *Nanoscale*. 2013;5(21):10461-10471.
  22. Ullah R, Dutta J. Photocatalytic degradation of organic dyes with manganese-doped ZnO nanoparticles. *Journal of Hazardous Materials*. 2008;156(1-3):194-200.
  23. Abdollahi Y, Abdullah AH, Gaya UI, Zainal Z, Yusof NA. Enhanced photodegradation of o-cresol in aqueous Mn(1%)-doped ZnO suspensions. *Environmental Technology*. 2012;33(10-12):1183-1189.
  24. Lu Y, Lin Y, Xie T, Shi S, Fan H, Wang D. Enhancement of visible-light-driven photoresponse of Mn/ZnO system: photogenerated charge transfer properties and photocatalytic activity. *Nanoscale*. 2012;4(20):6393-6400.
  25. Chen Z, Li Y, Guo M, Xu F, Wang P, Du Y, et al. One-pot synthesis of Mn-doped TiO<sub>2</sub> grown on graphene and the mechanism for removal of Cr(VI) and Cr(III). *Journal of Hazardous Materials*. 2016;310:188-198.
  26. Deng QR, Xia XH, Guo ML, Gao Y, Shao G. Mn-doped TiO<sub>2</sub> nanopowders with remarkable visible light photocatalytic activity. *Materials Letters*. 2011;65(13):2051-2054.
  27. Tan J, Zhang W, Lv YH, Xia AL. Facile preparation of Mn-doped CeO<sub>2</sub> submicrorods by composite-hydroxide-salt-mediated approach and their magnetic property. *Materials Research*. 2013;16(4):689-694.
  28. Murugan B, Ramaswamy AV, Srinivas D, Gopinath CS, Ramaswamy V. Nature of manganese species in Ce<sub>1-x</sub>MnxO<sub>2-d</sub> solid solutions synthesized by the solution combustion route. *Chemistry of Materials*. 2005;17(15):3983-3993.
  29. Van Overstraeten RJ, Mertens RP. Heavy doping effects in silicon. *Solid State Electronics*. 1987;30(11):1077-1087.
  30. Pavan Kumar CHSS, Pandeewari R, Jeyaprakash BG. Structural, morphological and optical properties of spray deposited Mn-doped CeO<sub>2</sub> thin films. *Journal of Alloys and Compounds*. 2014;602:180-186.
  31. Spanier JE, Robinson RD, Zhang F, Chan SW, Herman IP. Size-dependent properties of CeO<sub>2-y</sub> nanoparticles as studied by Raman scattering. *Physical Review B*. 2001;64(24):245407.
  32. Fernández-García M, Martínez-Arias A, Hanson JC, Rodriguez JA. Nanostructured oxides in chemistry: characterization and properties. *Chemical Reviews*. 2004;104(9):4063-4104.
  33. Cong CJ, Liao L, Liu QY, Li JC, Zhang KL. Effects of temperature on the ferromagnetism of Mn-doped ZnO nanoparticles and Mn-related raman vibration. *Nanotechnology*. 2006;17(5):1520.
  34. Choi WY, Termin A, Hoffmann MR. The role of metal ion dopants in quantum-sized TiO<sub>2</sub>: correlation between photoreactivity and charge carrier recombination dynamics. *The Journal of Physical Chemistry*. 1994;98(51):13669-13679.